

An Evaluation of H13 Tool Steel Deformation in Hot Forging Conditions

J. Marashi^{1,a}, E. Yakushina^{2,b}, P. Xirouchakis^{1,c}, R. Zante^{2,d}, J. Foster^{2,e}

¹*DMEM, University of Strathclyde, United Kingdom;* ²*Advanced Forming Research Centre, United Kingdom*

^ajames.marashi@strath.ac.uk, ^bevgenia.yakushina@strath.ac.uk, ^cpaul.xirouchakis@strath.ac.uk,

^dremi.zante@strath.ac.uk, ^ejim.foster@strath.ac.uk

Plastic deformation is one of the causes of failure of hot forging tools, where the tool deforms to such an extent that parts formed are no longer within dimensional tolerance. Therefore, deformation of H13 tool steel that leads to transformation of the microstructure after forging Inconel 718 at high temperature and load was investigated. For this investigation nonlinear continuum mechanics 3D FE simulation Deform software, Scanning Electron Microscope (SEM), Electron Backscatter Diffraction (EBSD) and Microhardness tests were used. The result of 3D Deform simulation shows high localised stress and high strain of 0.38 on the sharp edge of the tool. This is one of the main reasons behind tool failure as accumulation of strain during deformation at high temperature causes changes in microstructure. SEM results confirm the severe deformation and highlight three different zones of deformation, recrystallization, martensitic and transition between each zone within the microstructure. EBSD results show low angle boundaries of $1\sim 15^\circ$ which represents mainly the deformation zone and it is associated with different dislocation substructures caused by slip. Furthermore, misorientation angles $28\sim 32^\circ$ corresponds to special boundaries $\Sigma 39a$ which are believed were created during martensitic lattice transformation when some of the boundaries are not perfectly match the rest. These special boundaries transform to low angle boundaries. The high angle boundaries $58\sim 60^\circ$ corresponds to twin boundaries and their parent matrix.

Keywords: H13 tool steel, deformed microstructure, hot forging, martensitic transformation, recrystallization, microhardness.

1. Introduction

H series steels are usually used for manufacturing dies with properties capable of withstanding the high loads and temperatures of forging. These types of steel, upon being double or triple tempered at $566\sim 594^\circ\text{C}$, develop a combination of high hardness, high ultimate tensile strength, good fracture toughness and maximum fatigue strength at room and elevated temperatures (Benedyk J.C 2008). H13 tool steel has the second highest percentage of chromium compared to other H series and average amounts of vanadium and molybdenum, making it suitable for hot forging. High chromium content increases the resistance to high temperature and oxidation, molybdenum increases the hardenability. Vanadium increases the strength, toughness and improves fabrication and service performance. Tool steels are tempered to near maximum hardness at which they have sufficient toughness to withstand loading (ASM International Edited by Prasad Y.V.R.K, Rao K.P, Sasidhar S 1993). Therefore hardened H13 tool steel, with hardness of 53 HRC (Rockwell C) was used to withstand the load and high temperature of forging Inconel 718 billets at temperature of 1050°C . Increasing the hardness of tool steel increases the wear resistance and hot strength but it lowers the impact strength. Table 1 shows the result of X-ray fluorescence non-destructive analytical technique that was used to identify the chemical composition of the tempered H13 tool which was used in experiment.

As much as die material selection is important in protecting the die from the failure, workpiece material selection also has a huge influence on tool life because of interaction between the two materials. Nitriding and surface coating can improve die resistance to wear, deformation, heat checking, thermal fatigue and mechanical fatigue by increasing surface hardness and reducing the friction between die and work piece (Roberts et al. 1998), (Dennis

and Mahmoud 1987). For the project hardened H13 tool steel without nitriding or coating layer was used in order to investigate the deformation behaviour of H13 tool steel. A four piece die set, including top die, bottom die, insert and end stop was used (Fig. 1). The radius of the fillet on the insert was 1.5 mm.

200 Inconel 718 billets were heated for 15 minutes at 1050 °C and forged on H13 tool steel insert, which was heated up to 230 °C. Following the forging cycle, the insert showed evidence of deformation and adhesion (Fig. 2b). Forging dies deform elastically during the forging process. However, plastic deformation is irreversible and results in die failure (Douglas and Kuhlmann 2000). Therefore further investigation was necessary to understand H13 tool steel behaviour under elevated temperature and excessive load (Miland and Panasiuk 1982). The understanding of the non-uniform deformation and work hardening of the material is of critical importance.

Deformation at high temperature on the tool is down to the localise stress and strain and increase of dislocation density which initiates the recrystallization (Qian et al. 2011). Tempered hot work tool steels microstructure (i.e. tempered H13) consist of tempered martensite with high dislocation density (Medvedeva et al. 2009). This piece of work is devoted to investigating the deformation on hardened H13 tool steel by using different types of analysis including nonlinear continuum 3D FEM simulation, Vickers microhardness analysis, SEM and EBSD analysis.

2. Experimental methods

- X-ray fluorescence non-destructive analytical technique

X-ray fluorescence analysis was used to investigate the chemical composition of the adhesive layer on H13 tool insert.

- Five steps were taken in order to confirm plastic deformation and the reason behind it.
 - 1) Simulation

The first step was to perform an elastoplastic simulation using 3D Deform software. Nonlinear continuum mechanics allows large deformation. Linear continuum mechanics is valid for processes with a small strain and therefore small deformation (Bonet and Wood 1997). The flow stress data for H13 tool steel was taken from tensile tests which were performed at the AFRC (Advanced Forming Research Centre in Inchinnan) by Anderson et al (Anderson et al. 2013) for strain rates of 0.01s^{-1} and 0.1s^{-1} at a temperature range of 250-650 °C using Zwick/Roell Z250 machine. E21 ASTM standard was followed for the test using samples with the dimension shown on Fig. 3. The

samples were cut using EDM from the same material which was used for the tool. The flow stress data was extrapolated by the author up to a strain of 0.5 using the power law.

The flow stress model of Tabular data format was used (equation 1) on the simulation in which flow stress is function of effective plastic strain, effective strain rate and temperature.

$$\bar{\sigma} = \text{Flow stress}, \quad \bar{\sigma} = (\bar{\epsilon}, \dot{\bar{\epsilon}}, T) \quad (1)$$

$\bar{\epsilon}$ = Effective plastic strain,

$\dot{\bar{\epsilon}}$ = Effective strain rate,

T = Temperature.

Hardness values for different temperatures were taken from the literature (Benedyk J.C 2008). Tetrahedral mesh size of 0.6 mm was used on the contact area to increase the accuracy of the simulation. The Euler-Lagrangian incremental procedure where mesh node point moves with corresponding material points was used (Euler-Lagrange 2008). The simulation was run in two steps to consider loading and unloading. An elastoplastic simulation model (elastoplastic die and plastic billet) was used for the simulation. The billet temperature was set at 1050 °C and the bottom die temperature to 230 °C, while Top die temperature set at 250 °C. The reason behind the temperature differences between top and bottom bolster is the mechanical setup of Schuler screw press to prevent jam between the bolsters. The screw press works based on the energy input so 16KJ which is equivalent to 10 % of the total 160KJ capability of screw press was used. Die material data was taken from the result of tensile tests. The billet material data was taken from the Deform data base. The friction coefficient of 0.3 and heat transfer coefficient of 11 N/sec/mm/°C was used. The bottom die was constrained on the Y axis.

2) SEM imaging analysis

Two metallographic samples were prepared from deformed and non-deformed inserts. The fillets of the inserts were cut then both samples were mounted, ground and polished without etching. Both samples were investigated in a SEM (Quanta FEG 250) in turn to produce a backscattered electron (BSE) image from the highlighted area. The Fig. 4a shows the fillet of the insert which was cut using EDM and Fig. 4b shows the area of interest on the sample.

3) EBSD analysis

After taking SEM images from both of the samples, the EBSD analysis (HKL system) have been carried out. For EBSD investigations 15 kV voltage, scanning step size of 0.2 μm and 4 \times 4 binning were chosen. The exact area shown on Fig. 4 was selected for EBSD analysis eliminating the resin mounted area.

4) Microhardness test

A Dura Scan 70 G5 Vickers microhardness tester was used to characterise local scale hardness distribution. 25 hardness measurements (5 \times 5 matrix) were taken at depth of 0.6 mm from the edge of the sample using 0.12 mm between each indentation with applied force of 0.5 kgf. The schematic on Fig. 5 shows the patterns for hardness test.

5) Thermal camera

A Land thermal camera with temperature range of 0-500 $^{\circ}\text{C}$ and ± 2 $^{\circ}\text{C}$ accuracy (Thermal and Imaging 1832) was used to monitor the change in temperature on H13 tool steel.

3. Results and discussion

3.1 XRF (X-ray fluorescence)

XRF result on Table 2 shows the chemical composition of H13 tool after forging. 5.4 (Wt. %) of Ni in particular proves that the transferred asperity from Inconel 718 billets were attached to the H13 insert. As when two solid surfaces are in contact, the interfacial bond may be stronger than the cohesive bond in the cohesively weaker of the two materials. In that case, on separation of the two solids, this results in the transfer of the cohesively weaker material to the cohesively stronger (Bhushan B 2013). As the focus of this work is on the deformation therefore the rest of this work has been devoted on investigating the deformation of H13 tool steel.

Deformation analysis results:

3.2 Simulation

After executing the elastoplastic simulation, one point on the stress concentration area was selected for loading and unloading part of the simulation using Deform 3D postprocessor as shown on Fig. 6.

The results obtained from the thermal camera shows that the die temperature rises in the range of 350-400 °C from the initial temperature of 230 °C (). The analysis carried out with thermal camera were performed for every individual forging blow after removing forged part from the insert from the same point as indicated on Fig. 6. Therefore, the result has been influenced by air cooling along with cooling caused by lubricants. An emissivity of 0.8 was used for recording the temperatures.

By knowing H13 die temperature during the forging process from thermal camera results, the yield point at this temperature was identified as 1100 MPa from H13 tensile test results as shown in Fig. 8. Fig. 8a is true stress-strain curve for tensile test at a strain rate of 0.1s^{-1} and temperature of 400 °C before extrapolation and Fig. 8b is the result for the same test after extrapolation to 0.5 strain using power law.

Therefore, from the stress strain curve in Fig. 8 and effective stress curve in Fig. 9 which was taken from the simulation result confirms that the material has yielded during forging process.

The simulation also shows a high plastic strain of 0.38 (Fig. 6) after one cycle of forging Inconel 718 on H13 tool steel. This high level of strain alongside with the thermal softening

can cause deformation all the way through the forging process. After hot deformation or during the dwell period between each blow or in final cooling, the material experiences recovery or recrystallization (McQueen 2007). Static recrystallization (SRX) occurs when new nuclei which are free from the strain form and grow to new grains at the expense of the deformed material (Zahiri & Hodgson 2004). The SRX happens when the strain level is below the critical strain for dynamic recrystallization. The critical microstructural condition, for example high dislocation density, which occurs when stress in some regions on the surface is much higher than the average stress in the lattice, promotes dynamic recrystallization (DRX). Under this condition new grains are nucleated and grow while deformation is progressing. When strain level reaches the critical strain, nuclei which have been formed as a result of DRX, progress to metadynamic recrystallization (MDRX) which occurs by constant growth of the nuclei formed by DRX during straining (Cho et al. 2001), (Sakai et al. 2014).

3.2 Microstructure analysis

The high strain achieved on the FE simulation shows that H13 tool steel has gone through deformation. To confirm the simulation results two samples were prepared from deformed and brand new tools. The same magnification was used and an image was taken from the same area to increase comparison accuracy. Fig. 10a shows tempered martensite microstructure which is expected as the tool was not used for any forging process. Fig. 10b shows BSE images were taken from the samples prior and after forging.

The magnified BSE image, including the evolution of the zones is depicted in

Fig. 11,

Where 1) deformation zone, 2) transition between deformation and recrystallization zone, 3) recrystallization zone, 4) transition between recrystallization zone and martensitic zone, 5) martensitic zone.

Fig. 12 shows tempered martensite EBSD map plus analysis and Fig.13 shows EBSD maps and analysis of the deformed, recrystallized and martensitic zones obtained at depth of 0.6 mm. In body centred cubic structures (bcc), slip direction normally occurs on planes of the type $\{101\}$ and principal slip direction is along the plane $\langle 111 \rangle$ (Piehler 2009). Fig. 12a shows the fully tempered martensite microstructure on before forging sample where different grain boundaries including special CSL boundaries of $\Sigma 39a$ were found. Fig. 12b shows misorientation angles distribution histogram on before forging sample.

Fig.13a shows different zones including deformation zone which has been transformed to recrystallized zone in some parts. Fig.13b shows the misorientation angles distribution on after forging sample, where increased fraction of the low angle boundaries (LAB) represents the deformation zone and this is associated with different dislocation

substructures caused by slip. Furthermore in the middle of misorientation angles graph, the peaks at 28-32° corresponds to special boundaries $\Sigma 39a$ which were created during martensitic lattice transformation when some of the boundaries are not perfectly matched to the rest and transforms to low angle and special boundaries. The high angle boundaries 58-60° correspond to twin boundaries (Qian et al. 2011). The result shows that deformation of the tempered martensite leads to the transformation of the initial low and high angle boundaries and formation of the sub structure elements. The excessive load and high temperature on screw press causes further increase in dislocation density and transformation of low angle boundary to high angle boundary which has a positive effect on nucleation of recrystallized grains. Comparison of the histograms depicted on Fig. 12c with Fig.13c shows an increase in some of the boundaries including $\Sigma 13a$ and $\Sigma 39a$ and decrease of $\Sigma 3$, $\Sigma 11$, $\Sigma 33$ and $\Sigma 41$ which could be formed due to the high temperature and high strain, as misorientation angle is strongly dependent on the strain during high temperature deformation (H.U et al. 2008).

The range of measured microhardness on not deformed tool (before forging) was 523-610 HV, while measured microhardness on the deformed tool shows completely a different range 301~600 HV. The results of the microhardness measurements on the deformed tool confirm the evolution of the microstructure and formation of the different zones. Fig.14a showing the hardness colour map showing the change of microhardness in different zones and Fig.14b shows comparison between the change of microhardness before forging and after forging. It is clear that microhardness increases as indentation moves away from the edge of the sample.

Hardness measurement on pre-forging sample shows values of around 550-600 HV which indicates the suitability of this material under high thermal and load working conditions. As microhardness level depends on the microstructure in the measurement area, the non-uniform microhardness distribution confirms therefore the existence of different microstructure zones. The microhardness of as-quenched martensitic steels is strongly dependent on carbon content, especially for low- and medium-carbon steels. The low carbon content of 0.38 % (Table 1) confirms the insignificant to zero percentage of retained austenite which increases the microhardness. The microhardness could be preserved by the tempering at low temperature around 150-200 °C as it was shown in (Vlassak Joost.J, Nix W. D. 2016).

4. Conclusions

Investigations of the deformed H13 tool steel after forging of the Inconel 718 billets at high temperature and load showed a high localised stress and high strain of around 0.38 on the sharp edge of the insert. The SEM investigation confirms the deformation of the insert and highlights three different zones, deformed, recrystallised and martensitic, as well as

transition zones between each zones within the microstructure. The EBSD results show a large fraction of LAB which represents the deformation zone and it believed to be associated with different dislocation substructures caused by slip, while the 28-32° angles corresponds to special boundaries $\Sigma 39a$. The $\Sigma 39a$ boundaries were created during martensitic transformation. The HAB 58-60° corresponds to the twin boundaries. Comparison of the EBSD results before and after forging sample showed an increase of $\Sigma 13a$ and $\Sigma 39a$ boundaries and decrease of $\Sigma 3$, $\Sigma 11$, $\Sigma 33$ and $\Sigma 41$ which is due to microstructure transformation caused by excessive load and high temperature and the fact that orientation angle is strain dependant. Further work need to be done looking at effect of nitriding, and changing the tool design in order to minimise the stress concentration on the sharp edges which are more susceptible to deformation.

Acknowledgment

This work was supported by High Value Manufacturing Catapult (The Oracle Building, Blythe Valley Business Park, Shirley, Solihull, B90 8AD) established by the Innovate UK and The Advanced Forming Research Centre, University of Strathclyde (85 Inchinnan Drive, Renfrewshire, PA4 9LJ, United Kingdom).

References

1. Anderson M.J. et al., 2013. Identifying the dominant failure mode in the hot extrusion tooling used to forge nickel based superalloy. *Journal of Materials Processing Technology*, 213(1), pp.111–119.
2. ASM International Edited by Prasad Y.V.R.K, Rao K.P, Sasidhar S, 1993. ASM Forming and Forging. , 14(9 Edition), pp.80–90.
3. Benedyk J.C, 2008. *High performance Alloys Database (H13)*.
4. Bhushan B, 2013. *Introduction to Tribology 2 Edition.*, pp.158
5. Bonet J, Wood R.D, 1997. Nonlinear continuum mechanics for finite element analysis, *Cambridge University Press*, pp.20-49
6. Cho S.H, Kang K.B, Jonas J.J, 2001. The dynamic, static and metadynamic recrystallization of a Nb-microalloyed steel. *ISIJ International*, 41(1), pp.63–69.
7. Dennis J.K, Mahmoud E.A.A.G., 1987. Wear resistance of surface-treated hot forging dies. *Tribology International*, 20(1), pp.10–17.
8. Douglas R, Kuhlmann D, 2000. Guidelines for precision hot forging with applications. , 98, pp.182–188.
9. Euler-lagrange T, 2008. The Lagrangian Method. *Introduction to Classical Mechanics With Problems and Solutions*, pp.2-20.
10. He H.U. et al, 2008. Relationship between boundary misorientation angle and true strain during high temperature deformation of 7050 aluminum alloy. *Transactions of Nonferrous Metals Society of China (English Edition)*, 18(4), pp.795–798.
11. Vlassak Joost.J, Nix. W.D, 2016. Measuring the Elastic Properties of Anisotropic Materials by Means of Indentation Experiments. *J. Mech. Phys. Solids*, Vol. 42, (September), pp.1223-1245
12. McQueen H.J., 2007. Static Recrystallization of Tool Steels 1 1. , pp.4458–4463.
13. Medvedeva A. et al., 2009. High-temperature properties and microstructural stability of hot-work tool steels. *Materials Science and Engineering A*, 523(1–2), pp.39–46.
14. Miland C, Panasiuk W, 1982. Increasing the life of forging tools: New materials, technologies and methods of investigation. *Journal of Mechanical Working Technology*, 6(2–3), pp.183–191.
15. Piehler H.R, 2009. Crystal-Plasticity Fundamentals. , 22(Ref 2), pp.6.
16. Qian L, Feng X, Zhang F, 2011. Deformed Microstructure and Hardness of Hadfield High Manganese Steel. *Materials Transactions*, 52(8), pp.1623–1628.

17. Roberts G, Krauss G, Kennedy R, 1998. Tool Steels: 5th Edition. , pp.227.
18. Sakai T. et al., 2014. Dynamic and post-dynamic recrystallization under hot, cold and severe plastic deformation conditions. *Progress in Materials Science*, 60(1), pp.130–207.
19. Landinstrument. ARC IMAGER. *Land thermal camera standard*, pp. 1832.
20. Zahiri S.H, Hodgson P.D, 2004. The static , dynamic and metadynamic recrystallisation of a medium carbon steel. *Materials Science and Technology*, 20, pp.458.

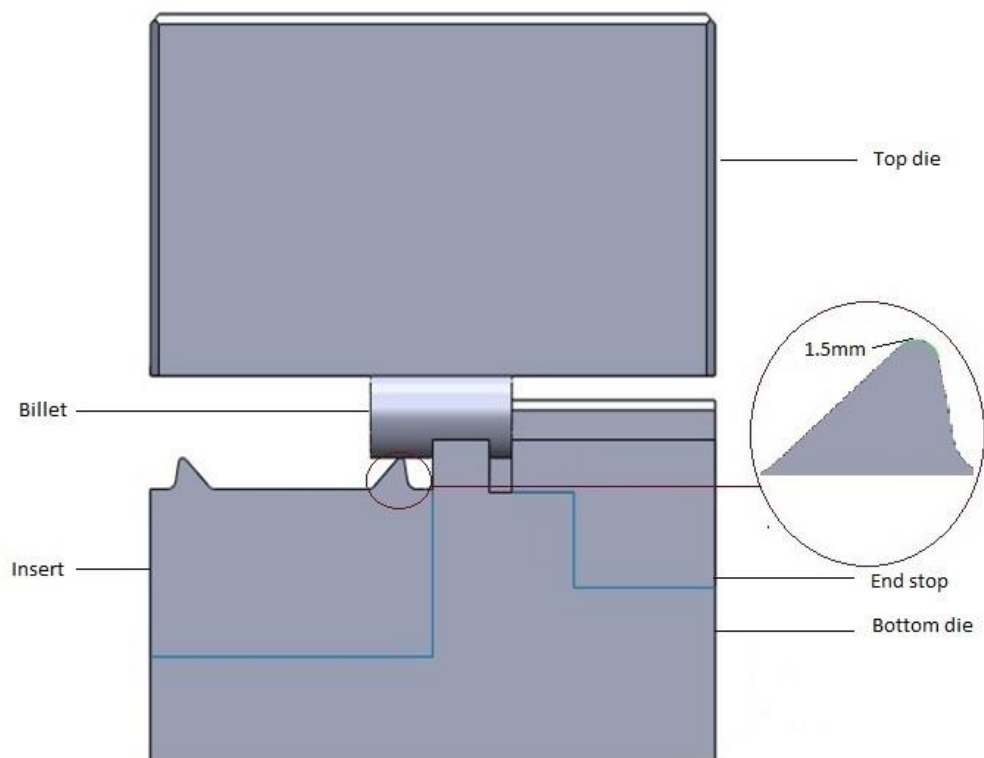


*Fig. 1 .
Four Piece die set consisting of Top die, Bottom die, Insert (with fillet radius of 1.5 mm) and End stop*

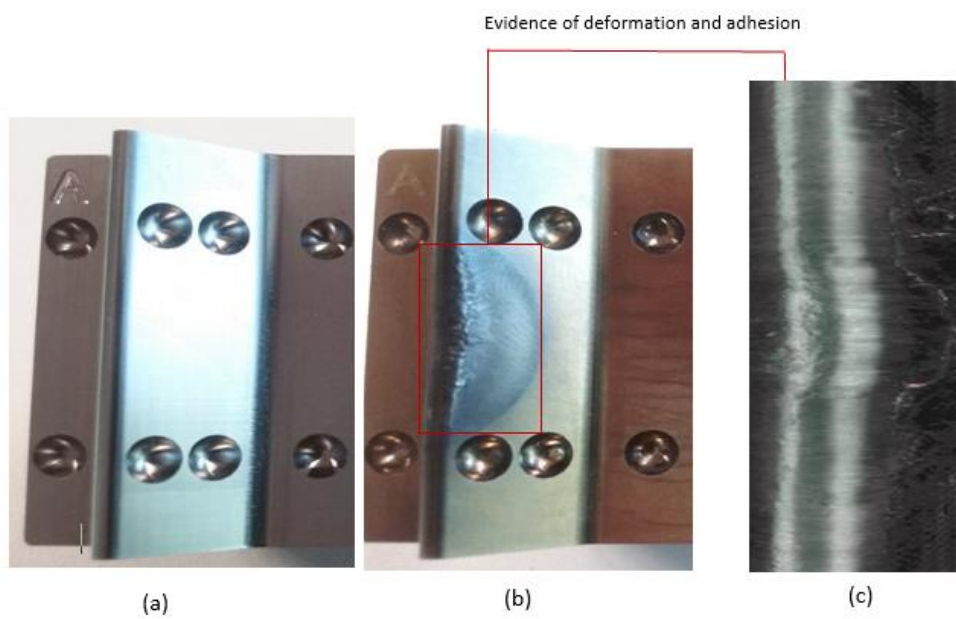


Fig. 2.
a) Insert image before forging, b) Insert image after forging showing evidence of deformation and adhesion, c) magnified area of the deformation and adhesion

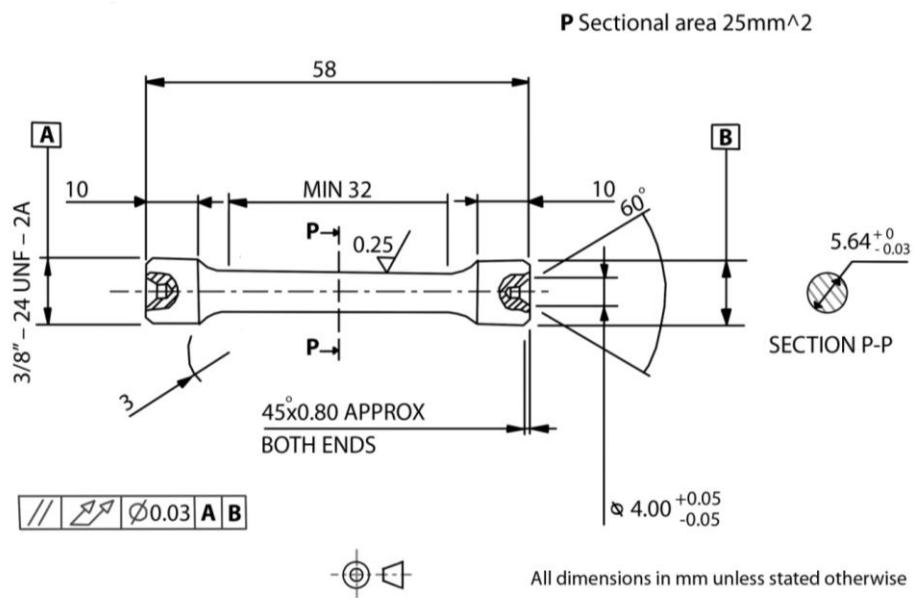


Fig. 3
Tensile sample dimensions (Anderson et al. 2013)

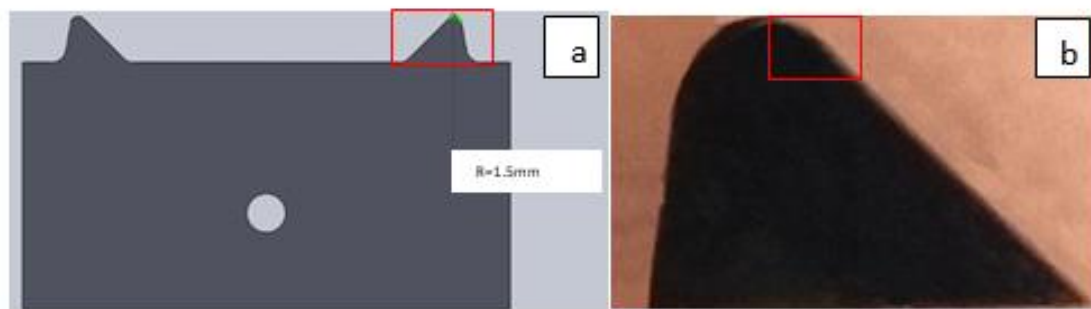


Fig. 4.

a) Fillet on the insert which was cut using EDM, b) Area of interest on the sample

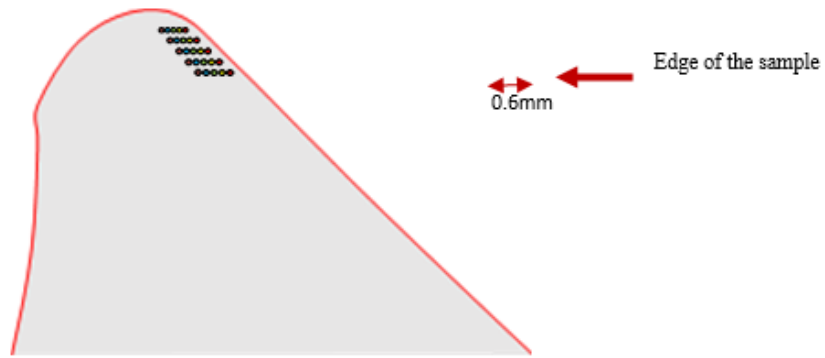


Fig. 5. Schematic of patterns for microhardness test performed on the fillet

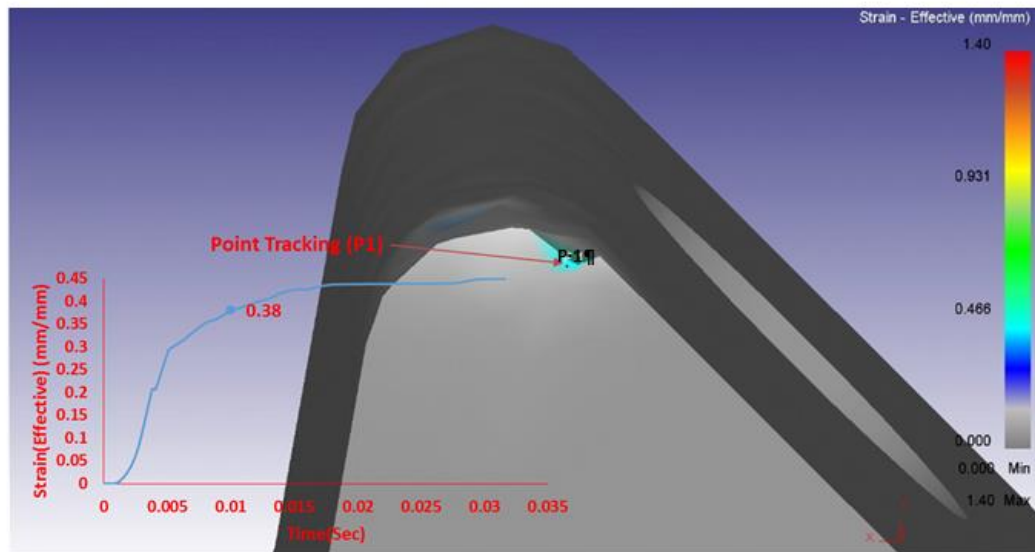


Fig. 6.
One point was selected with maximum stress concentration and high plastic strain of 0.38 on Deform 3D simulation post processor

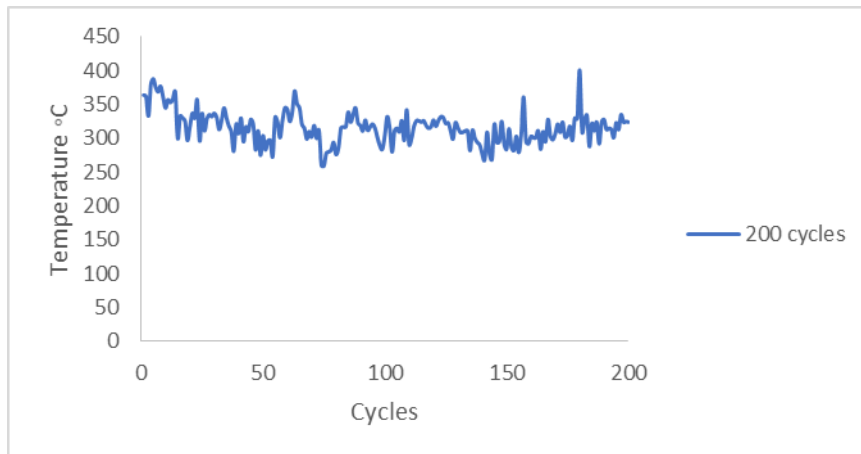


Fig. 7.
Land thermal camera results at emissivity of 0.8 (± 2 °C accuracy) for 200 cycles of forging (0.035 second for each cycle)

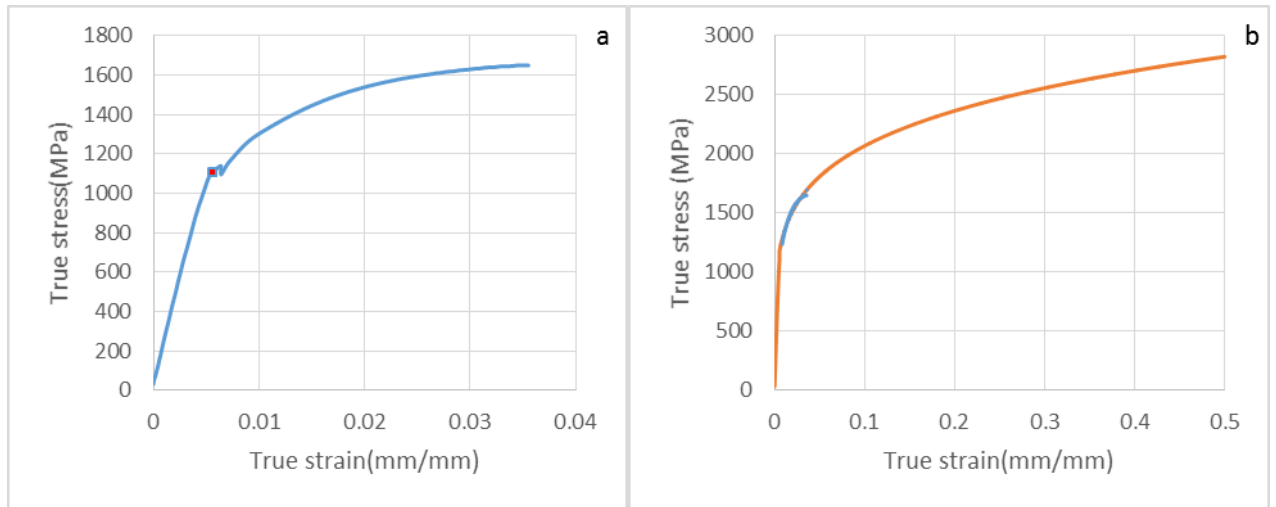


Fig. 8.

a) The tensile test at a strain rate $0.1s^{-1}$ and $400\text{ }^{\circ}C$ b) The result after extrapolation to 0.5 strain using power law for the same tensile test

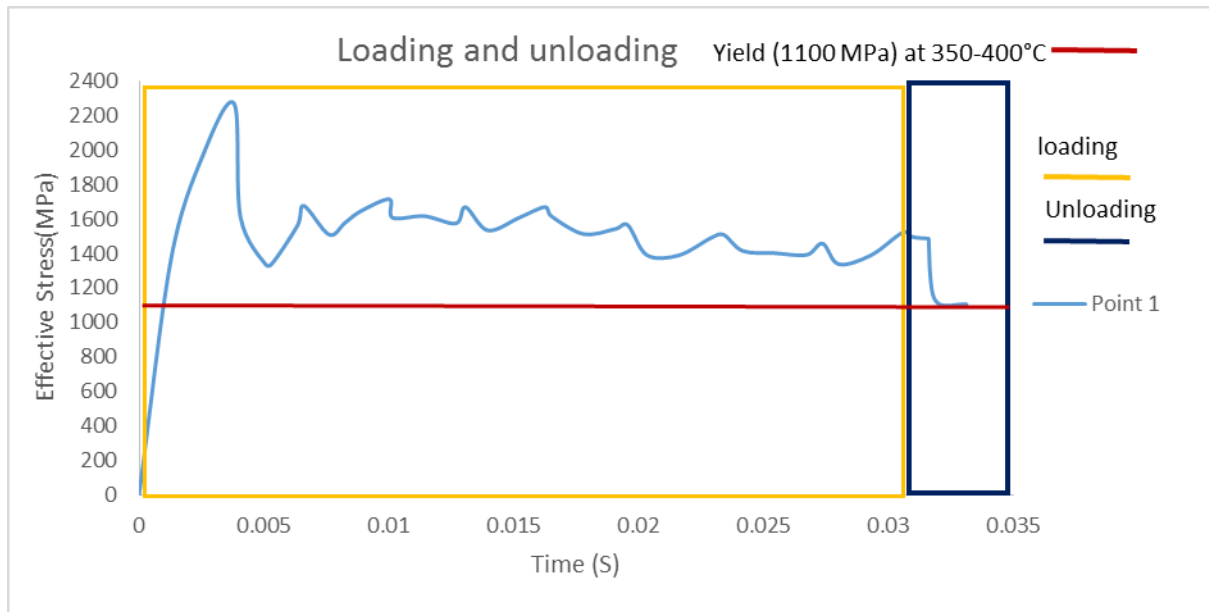


Fig. 9. Effective stress results from the simulation: an elastoplastic model shows that the yield stress of H13 tool steel was exceeded during forging

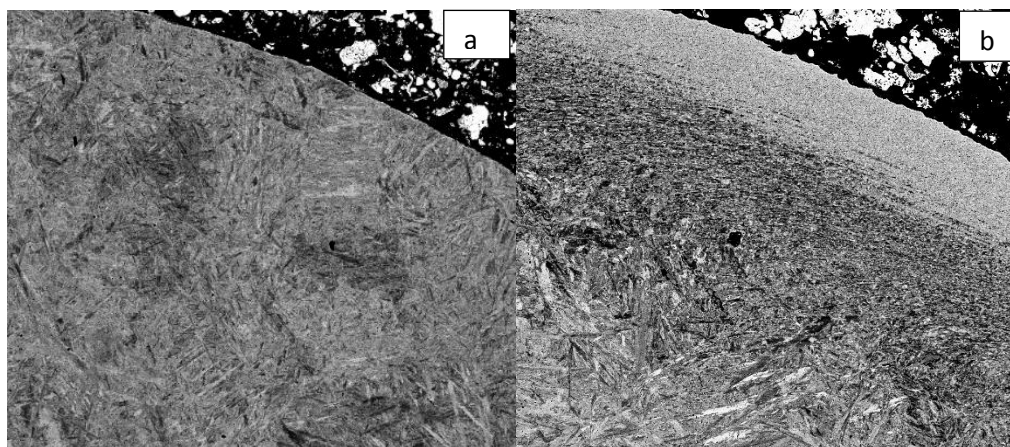


Fig. 10.
BSE images were taken from the samples: a) Before forging, b) After forging

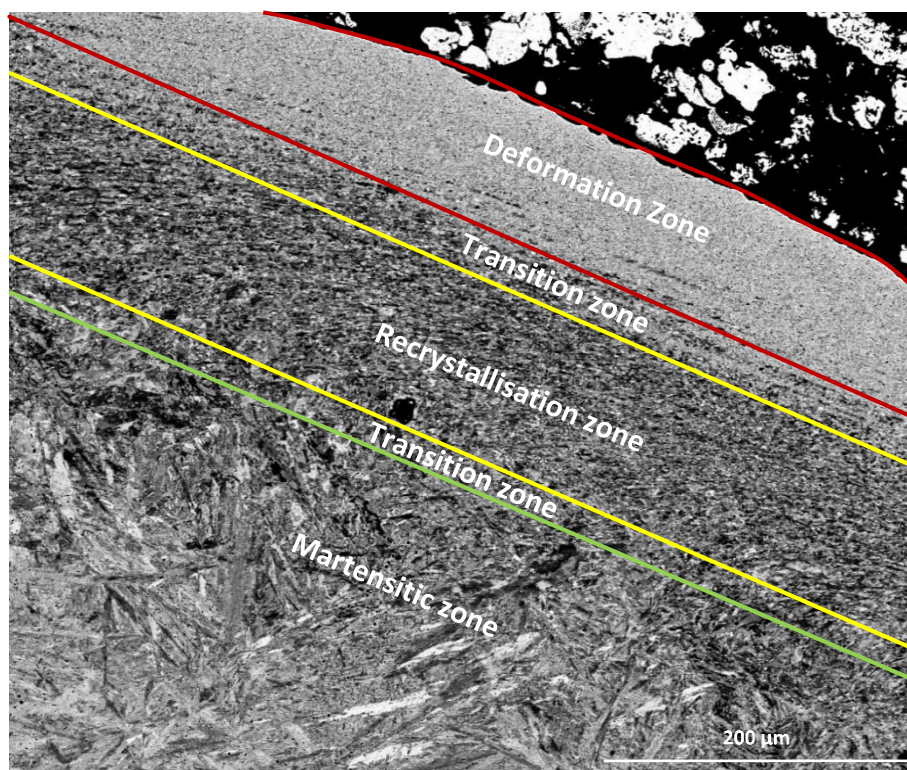
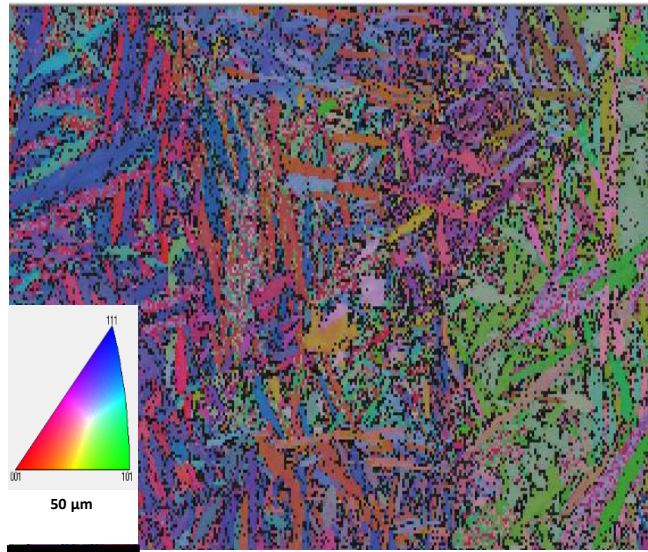
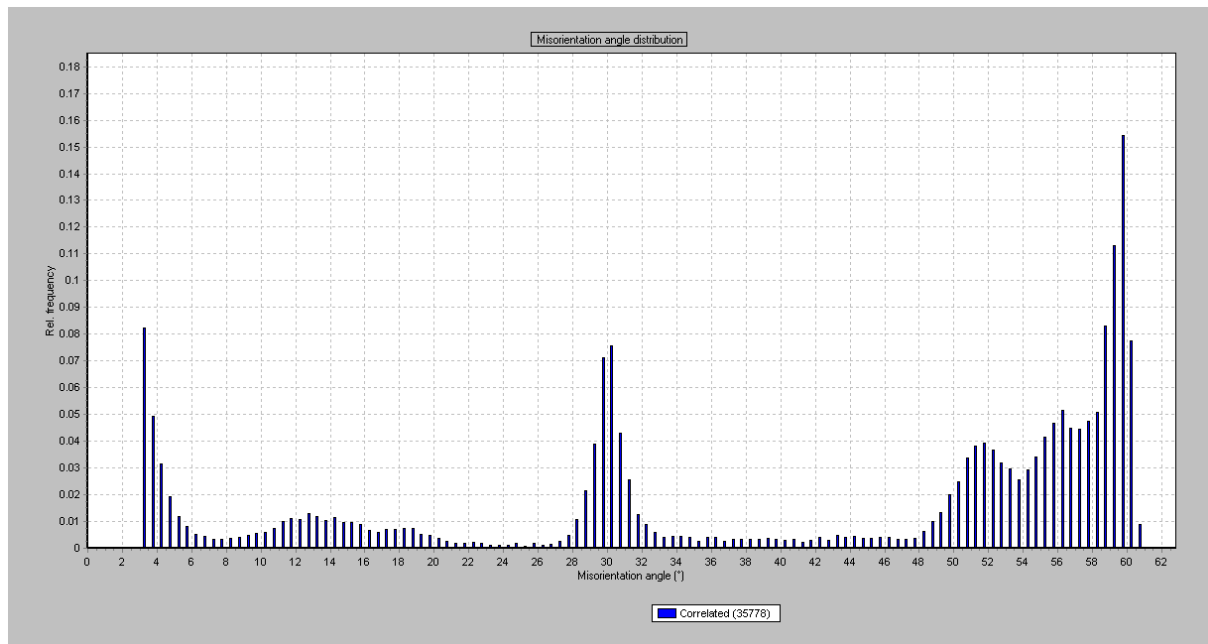


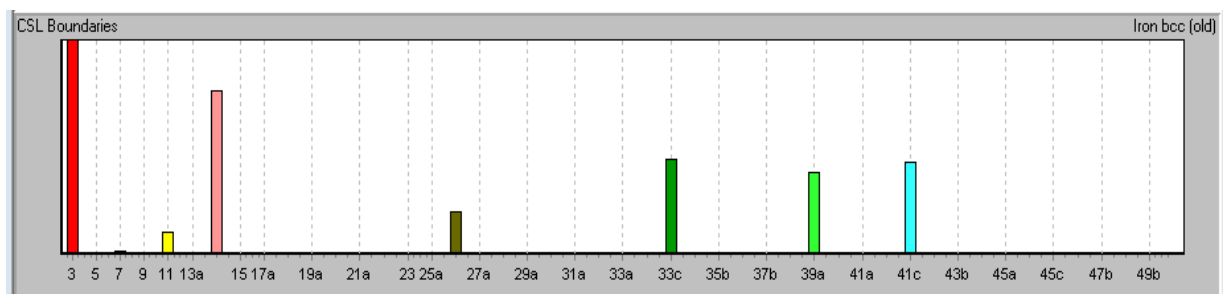
Fig. 11.
BSE image showing the evolution of Martensitic H13 Tool Steel microstructure after forging Inconel 718 billets at high temperature of 1050° C



a

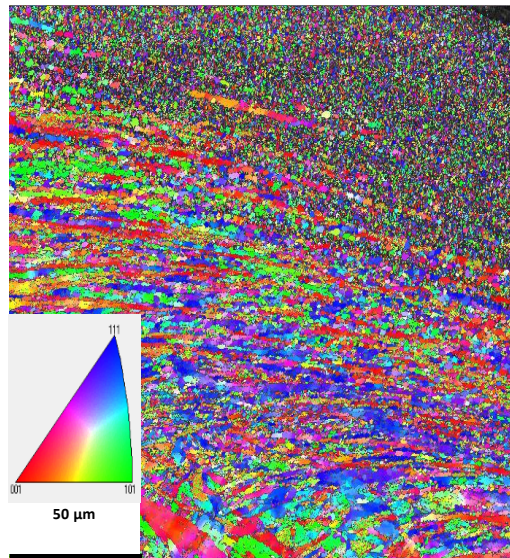


b

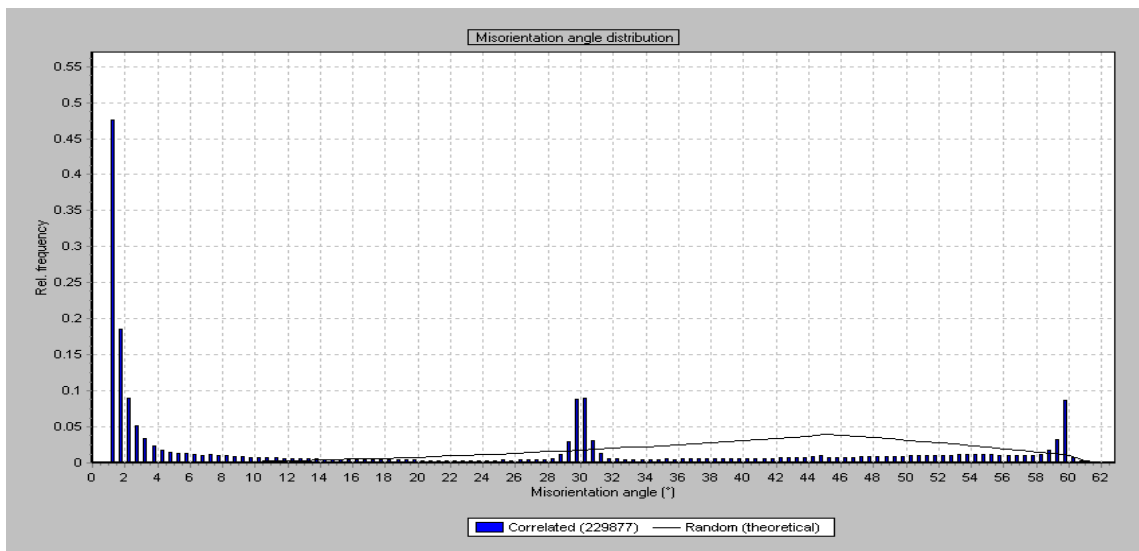


c

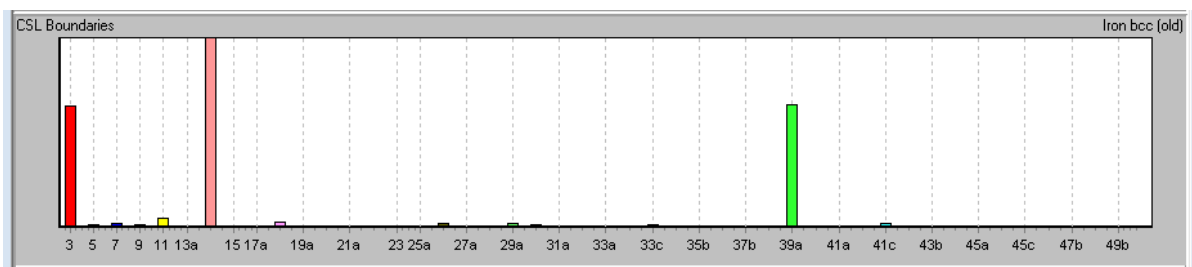
Fig. 12. a) IPF (Inverse pole figure) map which was obtained for the sample before forging, b) misorientation angles distribution histogram for the sample before forging, c) CSL (coincident site lattice) special boundaries distribution histogram for the sample before forging.



a



b



c

Fig.13.

a) IPF (Inverse pole figure) map which was obtained for the sample after forging, b) misorientation angles distribution histogram for the sample after forging, c) CSL (coincident site lattice) special boundaries distribution histogram for the sample after forging.

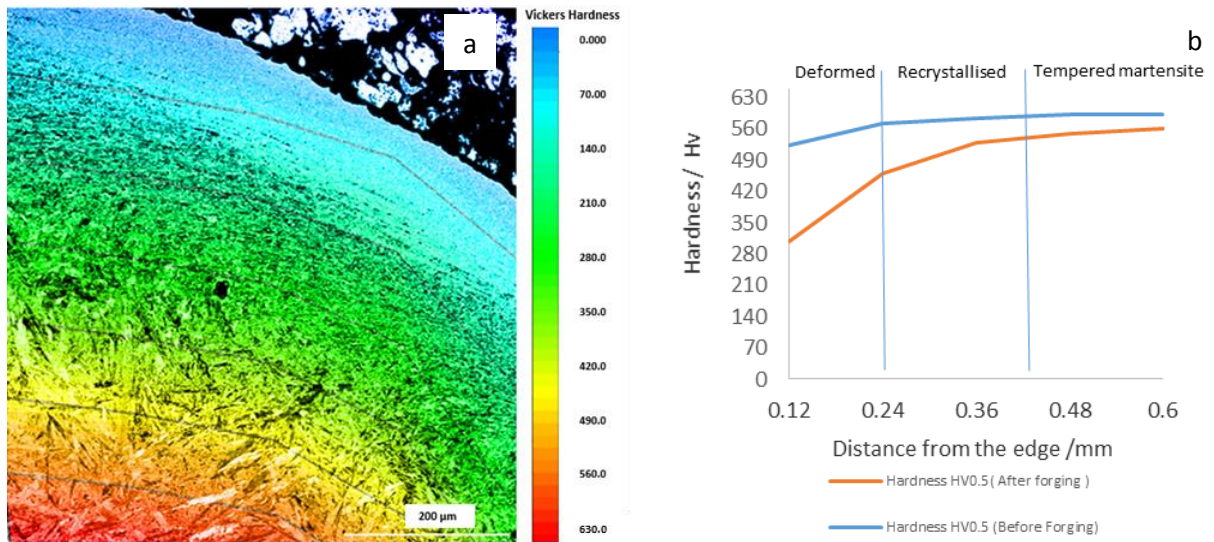


Fig.14.

a) The colour map showing change of microhardness in different zones and b) Comparison between microhardness levels achieved on before forging and after forging samples

Table 1: H13 nominal chemical composition (wt. %) compared to the result of X-ray fluorescence analysis

Conditions	C	Si	Mn	S	P	Cr	Mo	V	Fe
Nominal	0.37	1.03	0.45	0.0008	0.026	5.13	1.28	0.95	89
Measured by XRF	0.38	1.2	0.5	0.016	0.002	5.5	1.75	0.89	94

Table 2: H13 chemical composition after forging (Wt. %)

Si	Cr	Mn	Fe	Ni	Mo	V	Co	Cu
0.4	21.4	1.2	67.6	5.4	3.2	0.11	0.30	0.15